

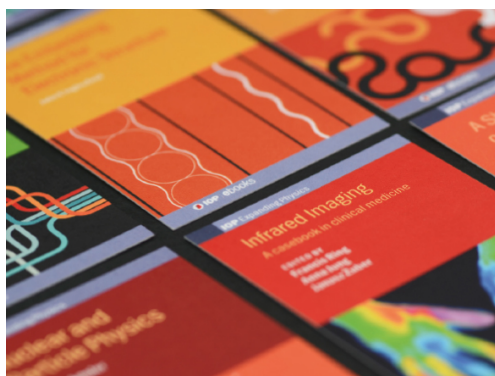
Prediction of melt pool depth and dilution in laser powder deposition

To cite this article: Alireza Fathi *et al* 2006 *J. Phys. D: Appl. Phys.* **39** 2613

View the [article online](#) for updates and enhancements.

You may also like

- [Laser-induced plume investigated by finite element modelling and scaling of particle entrainment in laser powder bed fusion](#)
Y A Mayi, M Dal, P Peyre *et al.*
- [Computer simulation of microstructure development in powder-bed additive manufacturing with crystallographic texture](#)
J G Pauza, W A Tayon and A D Rollett
- [A mesoscopic digital twin that bridges length and time scales for control of additively manufactured metal microstructures](#)
Tae Wook Heo, Saad A Khairallah, Rongpei Shi *et al.*



IOP | ebooks™

Bringing together innovative digital publishing with leading authors from the global scientific community.

Start exploring the collection—download the first chapter of every title for free.

Prediction of melt pool depth and dilution in laser powder deposition

Alireza Fathi¹, Ehsan Toyserkani^{1,3}, Amir Khajepour¹ and Mohammad Durali²

¹ University of Waterloo, Department of Mechanical Engineering, Waterloo, On N2L 3G1, Canada

² Sharif University of Technology, Mechanical Engineering Department, Tehran, Iran

E-mail: etoyserk@uwaterloo.ca

Received 5 April 2006, in final form 28 April 2006

Published 2 June 2006

Online at stacks.iop.org/JPhysD/39/2613

Abstract

This paper presents a mathematical model of laser powder deposition (LPD) to predict temperature field, melt pool depth and dilution. The model validated by experiments is developed using the moving heat source method. In this method, the temperature distribution inside the clad and the substrate is obtained using the superposition principle and the solution of the heat diffusion due to a point heat source. The model, which can be used in real-time applications, predicts the melt pool depth and dilution as a function of clad height and clad width, which in practice can be measured by a vision system. Numerical and experimental analyses show a non-linear behaviour of the melt pool depth as a function of process speed. This indicates that the melt pool depth has a maximum at a certain process speed. The comparisons between the numerical and experimental results show that this model is capable of predicting the characteristics of the LPD process accurately. Using the model, some general curves that show the behaviours of the melt pool depth and dilution as a function of clad height, scanning speed and laser power are illustrated.

(Some figures in this article are in colour only in the electronic version)

1. Introduction

Laser powder deposition (LPD) is an advanced laser material deposition technique, which has many applications such as coating [1], tools repair [2], rapid prototyping [3], manufacturing of functionally graded materials [3] and many others.

Despite numerous advantages of this method, its industrial applications are still limited. This is mainly because of a complex relationship among the process parameters (i.e. thermo-physical property of materials, laser power, process speed, powder flow-rate) and the process characteristics (i.e. clad geometry, cooling rate and material deposition rate). To produce a clad with good strength and minimum amount of porosity, crack, residual stress and dilution, the process characteristics should be monitored and controlled continuously.

Nowadays, with vision apparatus the clad geometry can be monitored and measured with good accuracy, whereas the metallurgical characteristics of the clad cannot directly be measured [1]. One of the possible methods for controlling and monitoring these characteristics is the application of a high fidelity numerical or experimental model.

In the literature, several analytical and numerical models have been proposed. In these models, the effects of important phenomena such as heat conduction, thermo-capillary flow, laser power attenuation due to powder flow and laser power absorption on the process characteristics have been demonstrated.

Picasso and Hoadley [4] proposed a two-dimensional, macroscopic, stationary finite element model for laser re-melting and laser cladding processes. They studied the effects of both thermo-capillary and powder injection force on the temperature distribution and velocity field inside the melt pool. Hoadley and Rappaz [5] presented a two-dimensional

³ Author to whom any correspondence should be addressed.

finite element model for studying the quasi-steady temperature field. In their study, they assumed that the powder was mixed rapidly and uniformly within the melt pool. Mazumder and Steen [6] studied the quasi stationary heat transfer problem for laser re-melting, glazing and welding by solving the heat transfer equation with a Gaussian heat source using finite difference techniques. Chan *et al* [7] developed a two-dimensional transient model for studying convective heat transfer and surface tension driven fluid flow. Their model was based on solving the energy and momentum equations. Han *et al* [8] developed a continuum model for coaxial laser cladding with powder injection. They took into account most of the physical phenomena involving processes such as melting, solidification and evaporation. They showed that the LPD process was a highly dynamic process. Toyserkani *et al* [9, 10] developed a 3-dimensional finite element model for the laser cladding process and studied the effects of powder feed rate, process speed and laser pulse shaping on the clad characteristics. They decoupled the contribution of additive materials and the thermal phenomena in their model. Pinkerton and Li [11] developed a mathematical model based on mass and energy balances for multi-layer LPD. They assumed arcs of circles for the melt pool geometry as opposed to the elliptical shape. Their model predicted the clad height and width at various given process parameters such as powder feedrate and power laser.

Since most of the proposed models were computationally intensive, they could not directly be used for real-time control applications. In this paper, we propose a model for predicting the melt pool depth, dilution and the temperature distribution over the process zone in the LPD process. The modelling approach starts with melt pool surface modelling in which, using known values of the clad height and the clad width, a surface for the upper shape of the melt pool is calculated. Then, by placing the heat source on this surface and solving the heat conduction problem, the lower shape of the melt pool that is in fact the boundary of the liquid phase and the solid phase is determined. The method of solving this heat conduction problem is based on using the solution of a moving point heat source and considering the superposition principle. In this method the temperature at each point is computed as a summation of the effect of each heat point source where the laser beam source is assumed to be an infinite number of heat point sources. The effects of Marangoni phenomena and phase changing are considered in the material properties. Using this model the effects of process speed and clad height on the melt pool depth and dilution are investigated and experimentally evaluated.

2. Mathematical model

For the LPD process, a moving laser beam with a known intensity profile melts the powder particles and a thin layer of the substrate. Figure 1 shows a schematic view of this process in which the powder is sprayed by a lateral nozzle into the process zone. As the figure shows, the laser beam strikes at the top surface of the melt pool. The laser power is attenuated by the powder particles through absorption, reflection and scattering the laser beam energy. When the attenuated laser beam reaches the melt pool surface, some portion of its power

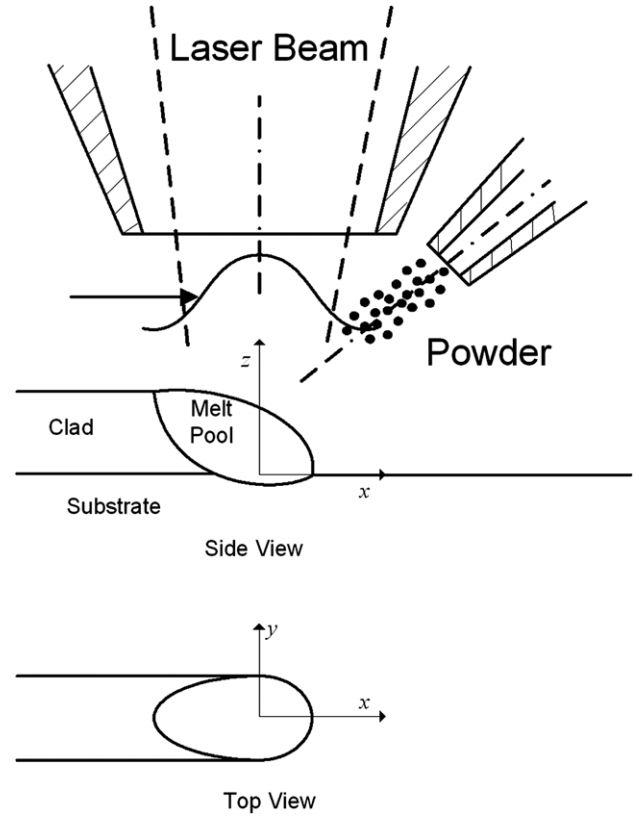


Figure 1. Schematic view of LPD.

is reflected and the remainder is absorbed. The absorbed power is carried away from the melt pool surface into the clad and substrate by the effects of thermal conduction and thermo-capillary (Marangoni) flow.

In this study, for simplification, the effect of the Marangoni flow is considered by a modified material thermal conductivity. Therefore, the problem of predicting the melt pool depth and dilution reduces to a heat conduction problem where the heat source is placed on the melt pool top surface.

2.1. Geometry of the upper melt pool surface

As mentioned before, the main goal of this modelling is to develop a model predicting the dilution in real time applications. Since the height and width of the melt pool can be measured by a vision system, it is assumed that they are given parameters. By knowing these values and considering a parabolic equation for the borders of the melt pool shown in figure 2, the following equations can be derived. According to figure 2(a), the upper melt pool surface can be modelled as

$$z = h(x)|_{y=0} = h_0 \left[1 - \frac{(x + L_2)^2}{(L_1 + L_2)^2} \right], \quad (1)$$

where $h(x)|_{y=0}$ is the melt pool height at the centre line of the clad (i.e. $y = 0$ and at point x), h_0 is the clad height (m), and L_1 and L_2 are dimensional parameters as shown in figure 2(a).

It is assumed that the clad height has a parabolic cross section (see figure 2(d)), and hence, the melt pool height at

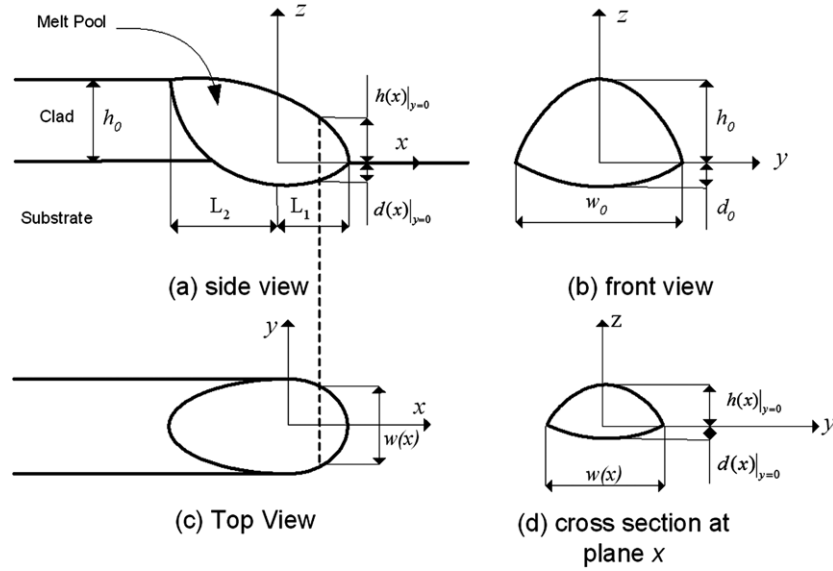


Figure 2. Melt pool surface modelling.

each point of (x, y) is obtained as

$$h(x, y) = h(x)|_{y=0} \left[1 - \frac{y^2}{w(x)^2} \right], \quad (2)$$

where $w(x)$ is the melt pool width at section x .

By considering a circular shape for the top view of the melt pool in $x > 0$ and a constant width for $x < 0$, $w(x)$ is obtained as

$$w(x) = w_0 \left[\text{sign}(-x) + \left(1 - \frac{x^2}{(w_0/2)^2} \right)^{1/2} \text{sign}(x) \right], \quad -L_2 \leq x \leq L_1 \quad (3)$$

where w_0 is the clad width (m) and sign is defined as

$$\text{sign}(x) = \begin{cases} 1 & x \geq 0 \\ 0 & x \leq 0. \end{cases} \quad (4)$$

2.2. Mathematical formulation

Figure 3 shows a schematic view of the heat conduction problem in a LPD process. As this figure shows, the moving laser heat source, which is assumed circular with a Gaussian intensity distribution, strikes the top surface of the melt pool. The quantity q_n^m represents energy supplied to the melt pool surface in (W m^{-2}) from the laser beam. Also the quantities q_n^s and q_n^c (W m^{-2}) represent heat losses from the substrate and the clad surface, respectively.

In order to obtain a close form solution for this heat conduction problem some simplifying assumptions are made as follows.

- (1) The material is isotropic and homogeneous.
- (2) The thermophysical properties are considered to be temperature independent and in this paper the mean values over the temperature range are taken. Since in this study the clad material is not the same kind of the substrate material, the mixture properties are used for thermal

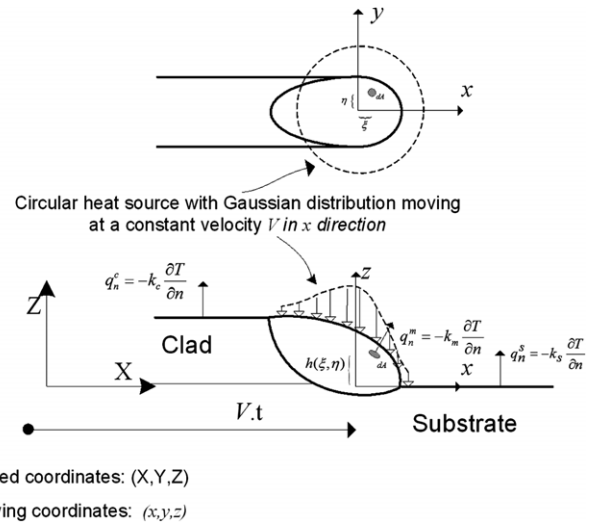


Figure 3. System and coordinates used in the modelling.

conductivity and thermal diffusivity as follows [8]:

$$K = f_c K_c + f_s K_s, \quad (5)$$

$$\alpha = f_c \alpha_c + f_s \alpha_s, \quad (6)$$

where K is the thermal conductivity (W mK^{-1}), α is the thermal diffusivity ($\text{m}^2 \text{s}^{-1}$), f_c and f_s are area fraction of the clad and the substrate in cross section plane, respectively.

- (3) The heat losses due to the radiation and convection to atmosphere are ignored. There are many studies that show that the magnitude of heat conduction to the substrate dominates other kinds of energy flow [11–13].
- (4) The laser power absorptivity is assumed not to vary with the angle of incidence of laser beam relative to the melt pool surface.

Since in this problem the heat flux q_n^m is known, the method of heat point source is applicable for solving the heat

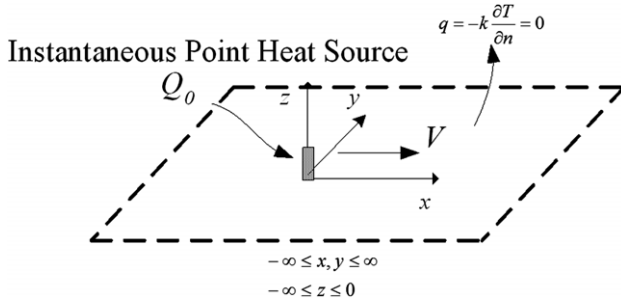


Figure 4. Heat conduction problem in the semi-infinite domain.

conduction problem. The basis for the heat point source method is the solution for the heat conduction into a semi-infinite work piece due to an instantaneous point heat source. Knowing this solution and considering the superposition principle, the temperature distribution due to a continuous heat source with a specific shape and intensity distribution can be computed where the heat source is considered to be an infinite number of point heat sources.

The solution for the heat conduction into a semi-infinite work piece due to instantaneous point heat source, which is located at $(x = 0, y = 0, z = 0)$ and moves with a constant speed V (m s^{-1}) along the x direction (see figure 4), can be expressed by [14]

$$T(x, y, z, t) = \frac{Q_0}{4\rho C_p (\pi \alpha t)^{3/2}} \times \exp\left(-\frac{(x + Vt)^2 + (y)^2 + (z)^2}{4\alpha t}\right) + T_0, \quad (7)$$

where $T(x, y, z, t)$ is the temperature (K), T_0 is the ambient temperature (K), Q_0 is the amount of instantaneously released energy (J), C_p is the specific heat capacity ($\text{J kg}^{-1} \text{K}$), ρ is the density (kg m^{-3}) and V is the heat source velocity (m s^{-1}).

If the heat is released at $q_0(t)$ (W) (i.e. $dQ_0/dt = q_0(t)$) from 0 to t , then the temperature rise can be obtained by considering the superposition principle. The temperature rise dT at point (x, y, z) at time t caused by the heat liberated in differential infinitesimally small time interval at time τ (using equation (7)) is given by

$$dT(x, y, z, t) = \frac{q_0(\tau) d\tau}{4\rho C_p (\pi \alpha (t - \tau))^{3/2}} \times \exp\left(-\frac{(x + V(t - \tau))^2 + (y)^2 + (z)^2}{4\alpha (t - \tau)}\right). \quad (8)$$

The total temperature rise caused by the moving point heat source can be obtained by integrating the above equation from $\tau = 0$ to t . If heat is released at a constant rate of q_0 then

$$T(x, y, z, t) = \frac{q_0}{4\rho C_p (\pi \alpha)^{3/2}} \times \int_{\tau=0}^t \frac{\exp(-((x + V\tau)^2 + (y)^2 + (z)^2)/4\alpha \tau)}{(\tau)^{3/2}} d\tau + T_0. \quad (9)$$

If $t \rightarrow \infty$, a steady state regime is established, and the temperature at (x, y, z) is [14]

$$T(x, y, z) = \frac{q_0}{2\pi K R} \exp\left(-\frac{V(R + x)}{2\alpha}\right) + T_0, \quad (10)$$

where $R = \sqrt{x^2 + y^2 + z^2}$ and K is the thermal conductivity (W m K^{-1}) which relates to α via $K = \rho C_p \alpha$.

Equations (9) and (10) are the basic solutions of the heat conduction equation with a moving source resulting in the temperature distribution due to a constant rate heat point source. Since in the LPD the heat source cannot be considered as a point source, the temperature rise is computed by integrating equation (10) over the laser beam area and on the upper surface of the melt pool.

To incorporate the effect of the laser beam shaping, it is assumed that the transverse mode of the laser beam is TEM_{00} and has a stationary Gaussian intensity profile as follows [15]:

$$I(r) = I_0 \exp\left(-\frac{r^2}{\sigma^2}\right), \quad (11)$$

where r is the distance from the laser centre point (m) and σ is calculated by

$$\sigma = \frac{\sqrt{2}}{2} r_b. \quad (12)$$

In equation (12) r_b is laser beam radius (m), and I_0 is the intensity scale factor (W m^{-2}) which is determined from

$$I_0 = \frac{\beta P_n}{\pi \sigma^2 \left[1 - \exp\left(-\frac{r_b^2}{\sigma^2}\right)\right]}. \quad (13)$$

In equation (13), β is the mean value of the laser power absorptivity, P_n is the average value of the laser power (W) which can be expressed as a function of laser pulse energy E (J) and laser pulse frequency F (Hz). In a pulsed laser P_n becomes

$$P_n = EF. \quad (14)$$

During LPD, heat is carried away from the melt pool surface into the clad and substrate by the effect of the two main phenomena: thermal conduction and thermo-capillary (Marangoni) flow [16]. The effect of Marangoni flow can be accounted for using a modified thermal conductivity. The experimental and numerical analysis show that the effective thermal conductivity in the presence of Marangoni flow is at least twice that of the stationary cases. This effect can be generally presented by [9]

$$K^* = aK \Big|_{T=T_m}, \quad \text{if } T > T_m, \quad (15)$$

where K^* is modified thermal conductivity ($\text{W m}^{-1} \text{K}^{-1}$), a is the correction factor and T_m is the melting point (K).

Also the effect of latent heat of fusion can be approximated by increasing the specific heat capacity as [17]

$$C_p^* = \frac{L_f}{T_m - T_0} + C_p, \quad (16)$$

where L_f is the latent heat of fusion (J kg^{-1}) and C_p^* is the modified specific heat capacity ($\text{J kg}^{-1} \text{K}^{-1}$).

According to figure 3, at point $(\xi, \eta, h(\xi, \eta))$ which is a point of the upper melt pool surface and considering a constant power absorptivity with respect to the angle of incidence of the laser beam relative to the melt pool surface, the heat flux from the laser that enters into the melt pool is

$$q_n^m = I(r) dA, \quad (17)$$

where $r = (\xi^2 + \eta^2)^{1/2}$, $dA = d\xi d\eta$ and ξ, η are the coordinates in the moving coordinate system.

It is possible to assume that this heat flux is a point heat source which is placed at $(\xi, \eta, h(\xi, \eta))$. Therefore, the temperature rise, dT , at point (x, y, z) and at time t due to this heat flux (using equation (9)) is

$$dT(x, y, z, t) = \frac{I(\sqrt{\xi^2 + \eta^2})d\eta d\xi}{2\rho C_p(\pi\alpha)^{3/2}} \times \int_{\tau=0}^{\tau=t} \exp\left(-\frac{\xi^2 + \eta^2}{\sigma^2}\right) \exp[-((x - \xi + V\tau)^2 + (y - \eta)^2 + (z - h(\xi, \eta))^2)/4\alpha\tau] \tau^{-3/2} d\tau. \quad (18)$$

The temperature at any point (x, y, z) caused by the total laser beam can be obtained by integrating equation (18) over the laser beam spot as follows:

$$T(x, y, z, t) = \frac{I_0}{2\rho C_p(\pi\alpha)^{3/2}} \times \int_{\xi=-r_b}^{\xi=r_b} \int_{\eta=-r_b}^{\eta=r_b} \int_{\tau=0}^{\tau=t} \exp\left(-\frac{\xi^2 + \eta^2}{\sigma^2}\right) \times \exp[-((x - \xi + V\tau)^2 + (y - \eta)^2 + (z - h(\xi, \eta))^2)/4\alpha\tau] \tau^{-3/2} d\tau d\eta d\xi. \quad (19)$$

In case of the steady state regime, the temperature distribution is determined by the following equation:

$$T^{st}(x, y, z) = \frac{I_0}{2\pi K} \int_{\xi=-r_b}^{\xi=r_b} \int_{\eta=-r_b}^{\eta=r_b} \frac{1}{R} \exp\left(-\frac{\xi^2 + \eta^2}{\sigma^2}\right) \times \exp\left(-\frac{V(R + (x - \xi))}{2\alpha}\right) d\eta d\xi, \quad (20)$$

where $R = ((x - \xi)^2 + (y - \eta)^2 + (z - h(\xi, \eta))^2)^{1/2}$.

It should be noted that the equations (19) and (20) are based on the semi-infinite medium solution and the isolated boundary conditions as shown in figure 4. The use of these equations, when the medium is not flat, is subject to a heat flux on the boundaries. This heat flux which is a function of clad geometry and laser beam power distribution is small and is ignorable in practical applications.

Also the heat fluxes q_n^c and q_n^s which are due to the heat loss from the clad and the substrate surface can be considered in the modelling as heat sources. Since the amount of this heat loss is small in comparison with the energy that enters into the melt pool, in this study, for simplification, it is ignored.

The lower melt pool shape can be calculated by considering the isotherm surface at melting point $T = T_m$. For simplicity, the steady state condition is considered. In this regime, the function of the isotherm curve at melting point $T = T_m$ and at plane $y = 0$ (the plane that the deepest melt point occurs) is computed as

$$\phi_{T_m1}(x_m, z_m) = T_m - \frac{I_0}{2\pi K} \iint \frac{1}{R} \exp\left(-\frac{\xi^2 + \eta^2}{\sigma^2}\right) \times \exp\left(-\frac{V}{2\alpha}(R + (x_m - \xi))\right) d\xi d\eta = 0, \quad (21)$$

where $R = \sqrt{(x_m - \xi)^2 + \eta^2 + (z_m - h(\xi, \eta))^2}$ and (x_m, z_m) is a point of the lower melt pool shape.

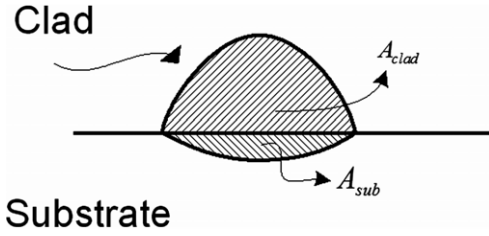


Figure 5. Cross section of the clad and substrate.

By considering equation (21) as the melt pool boundary at plane $y = 0$, the coordinate of the deepest point (x_m, z_m) can be obtained as

$$\frac{\partial \phi_{T_m1}}{\partial x_m} = 0, \quad (22)$$

which yields the following equation:

$$\phi_{T_m2} = \iint \left\{ \frac{V}{2\alpha} + \frac{1}{R} \left(\frac{V}{2\alpha} + \frac{1}{R^2} \right) (x_m - \xi) \right\} \exp\left(-\frac{\xi^2 + \eta^2}{\sigma^2}\right) \times \exp\left(-\frac{V}{2\alpha}(R + (x_m - \xi))\right) d\xi d\eta = 0. \quad (23)$$

By the simultaneous solving of equations (21) and (23), the deepest point of the melt pool (x_m, z_m) is determined.

Dilution is a very important factor in LPD. This parameter shows the amount of powder material dilution as a result of mixing with the substrate material. In this paper with an assumption of ideal mixing inside the melt pool, dilution is defined as (see figure 5)

$$\text{Dilution} = \frac{A_{\text{sub}}}{A_{\text{clad}} + A_{\text{sub}}}, \quad (24)$$

where A_{sub} and A_{clad} are the cross section areas of the substrate and the clad as shown in figure 5, respectively.

3. Numerical and experimental results

3.1. Experimental procedure

The experimental validation of the model was performed using a 1000 W LASAG FLS 1042N Nd: YAG pulsed laser, a 9MP-CL Sulzer Metco powder feeder unit and a 4-axis CNC table. The transverse mode of the laser beam was TEM₀₀ and the beam spot diameter on the workpiece was set to 1.4 mm where the laser intensity was Gaussian.

Powder was delivered to the processing point through a lateral nozzle, mounted at an angle of 29° relative to the laser beam axis. Argon gas was used for carrying the powder and also as a shield gas to shroud the process zone. It was also used to protect the optical lenses. The shield gas flow rate was set to 3 SCFH.

Stainless steel grad 303-L (Fe 70%:Cr 17%:Ni 13% wt%) with particle size of 50 μm was chosen as the material for powder and sandblasted mild steel plates (0.25–0.28% C; 0.6–1.2% Mn) with dimensions of 200 × 30 × 5 mm³ were used as substrates. The associated thermo-physical properties of the substrate used in this study are listed in table 1 [18]. For the thermal conductivity and thermal diffusivity the mean values over the temperature range were considered. The effective absorption factor for stainless steel was assumed to

Table 1. Thermo-physical properties of substrate and powder used in the numerical studies.

	Substrate	Powder
Thermal conductivity [$\text{W m}^{-1} \text{K}^{-1}$]	50 (25 °C)–30.0 (1200 °C)	28.2 (100 °C)–21.5 (1450 °C)
Specific heat capacity [$\text{J kg}^{-1} \text{K}^{-1}$]	481 (25 °C)–502 (1200 °C)	500 (25 °C)–800 (1500 °C)
Melting temperature [$^{\circ}\text{C}$]	1540–1595	1400–1450
Density [kg m^{-3}]	7830	7833–7920
Absorptivity [%]	44.9	44.9

Table 2. Laser processing properties.

Laser pulse energy	From 3 to 5 [J]
Laser pulse frequency	90 Hz
Laser pulse width	3 ms
Laser beam diameter	1.4 mm

Table 3. Conditions of experiments.

Test No.	E [J]	F [Hz]	W [ms]	V [mm s^{-1}]	\dot{m} [kg s^{-1}]
1	4	90	3	1.5	3.333e-5
2	4	90	3	2	3.333e-5
3	4	90	3	2.5	3.333e-5
4	4	90	3	3	3.333e-5
5	4	90	3	3.75	3.333e-5
6	4	90	3	5	3.333e-5
7	4	90	3	6.25	3.333e-5
8	4	90	3	7.5	3.333e-5
9	5	90	3	1.0	3.333e-5
10	5	90	3	1.5	3.333e-5
11	5	90	3	2	3.333e-5
12	5	90	3	2.5	3.333e-5
13	5	90	3	3	3.333e-5
14	5	90	3	3.75	3.333e-5
15	5	90	3	5	3.333e-5
16	5	90	3	6.25	3.333e-5
17	5	90	3	7.5	3.333e-5

be 44.9% [19] and the correction factor a is assumed to be 2.5 [10].

In order to validate the numerical results, several single track deposition experiments were tested using a range of different processing parameters. The associated laser parameters for these experiments are listed in table 2. Furthermore, table 3 lists the conditions of experiments. As this table shows, experiments were performed at different powers and velocities. In each experiment, a straight single track with 25 mm length was deposited. The produced clads were deposited on the centreline of the substrate which was at a distance of about 15 mm from the plate edge. To be consistent in the experiments, after each deposition, the substrate was allowed to reach room temperature before the next deposition took place.

The samples were cross-sectioned, mounted, polished and etched using nitric/hydrochloric solutions (2% Nital).

3.2. Results

To gain insight into the nature of the melt pool depth in the LPD process, several numerical and experimental analyses were carried out.

In figures 6 and 7, the experimental results of the clad height and the clad width in terms of scanning speed are plotted,

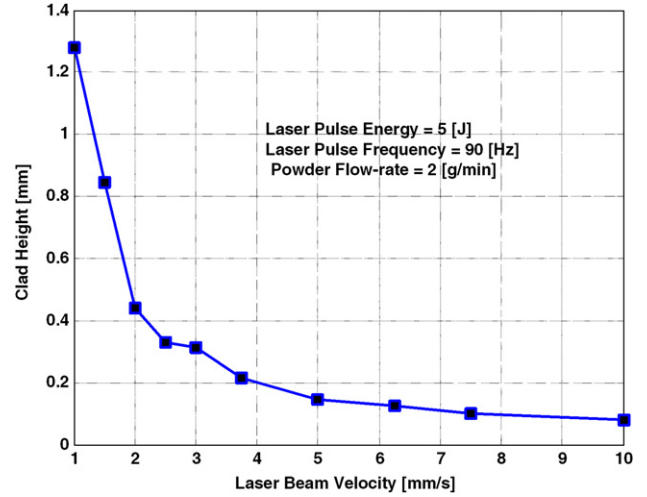


Figure 6. Experimental results of clad height variations with respect to scanning speed at $E = 5 \text{ J}$, $F = 90 \text{ Hz}$, $\dot{m} = 2 \text{ g min}^{-1}$.

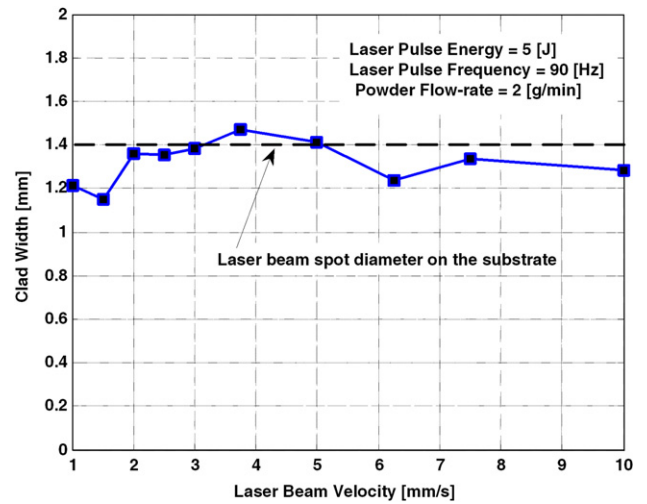


Figure 7. Experimental results of clad width variations with respect to scanning speed at $E = 5 \text{ J}$, $F = 90 \text{ Hz}$, $\dot{m} = 2 \text{ g min}^{-1}$.

respectively. As the figures show, at a fixed amount of laser power, the clad height reduces with increasing the scanning speed but the clad width remains relatively constant close to the laser beam diameter.

For measuring the melt pool depth, each of the produced clads are cross sectioned and measured as shown in figure 8. As the figure shows, the melt pool depth is not uniformly varied over the width of the clad. One reason for this nonuniform substrate/clad interface can be the Gaussian distribution of the laser beam, which, in turn, provides higher energy in the central part of the clad. Figures 9 and 10 show the comparison of the

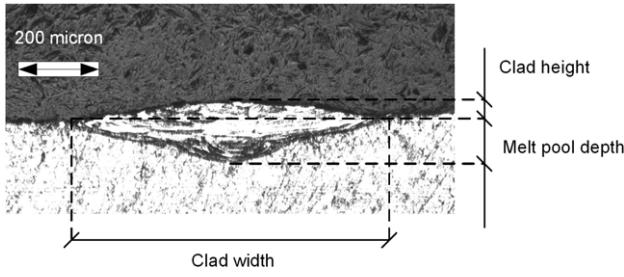


Figure 8. Clad cross section.

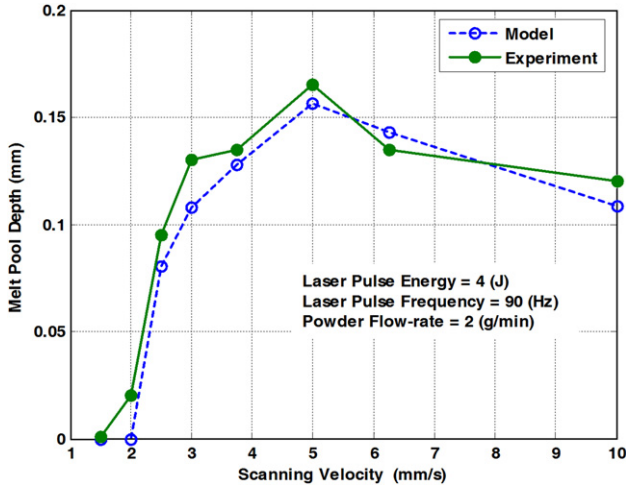


Figure 9. Comparison between the numerical and experimental results at $E = 4$ J, $F = 90$ Hz, $\dot{m} = 2$ g min⁻¹.

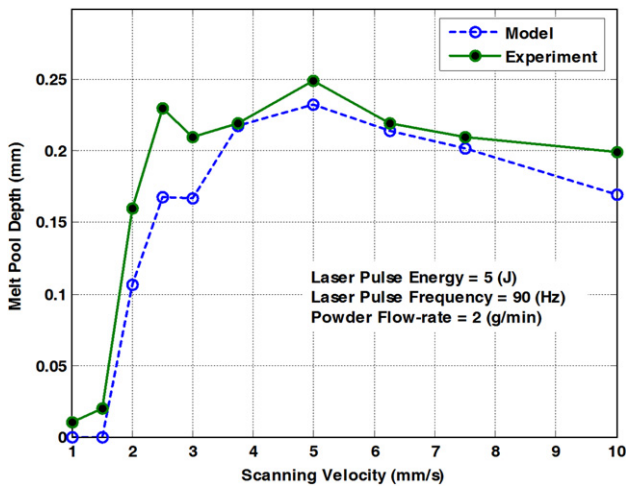


Figure 10. Comparison between the numerical and experimental results at $E = 5$ J, $F = 90$ Hz, $\dot{m} = 2$ g min⁻¹.

model output with the experimental data in predicting the melt pool depth as a function of scanning speed and at different laser power (i.e. $E = 4$ and 5 J). It should be noted that these results are based upon using the measured values of the clad height and clad width which are shown in figures 6 and 7 for $E = 5$ J. As these figures indicate, there is good agreement between the numerical and experimental results. The main reasons for the existing discrepancies are the deviation in the absorption factor, deviation in the powder feed-rate, increase in the angle

of incidence of the laser beam relative to the melt pool surface and deviation in material thermo-physical properties.

According to figures 9 and 10, a specific behaviour of the melt pool depth as a function of scanning speed is observed. The melt pool depth increases with increasing the scanning speed up to the critical value (i.e. 5 mm s⁻¹), then after the melt pool depth decreases with increasing scanning speed.

This specific behaviour of the LPD process can be explained by equations (19) and (20). In equations (19) and (20) a decrease in both the clad height and the scanning speed results in increasing the melt pool depth and vice versa. The decrease in the melt pool depth by increasing the clad height is a result of the shadowing (or blocking) effect. The shadowing effect refers to the phenomenon in which the formation of the melt pool blocks or reflects the incoming heat into the substrate, which in turn reduces the amount of the laser beam energy on the substrate. Also the decrease in the melt pool depth by the increase in the scanning speed is a result of the interaction time effect, so that at a higher scanning speed less energy enters into the substrate.

In summary, the interaction time and blocking effects impose a very interesting behaviour on the melt pool depth variations (see figures 9 and 10), so that at low scanning speed the clad height is relatively high and as a result of the blocking effect the melt pool depth is low. With increasing the scanning speed, the clad height decreases and therefore the melt pool depth starts increasing. At a critical scanning speed, the melt pool depth reaches its maximum. With increasing scanning speed the melt pool depth decreases, due to a shorter interaction time.

According to figures 9 and 10, for a fixed laser power, at velocities lower than 5 (mm s⁻¹) the blocking effect is dominant whereas at velocities greater than 5 (mm s⁻¹) the interaction time effect is the governing factor. This critical scanning speed can be obtained as follows.

The critical scanning speed V_{cr} can satisfy the following equation:

$$\left. \frac{\partial z_m}{\partial V} \right|_{V=V_{cr}} = 0. \quad (25)$$

Since z_m is not an explicit function with respect to V , the critical scanning speed can be obtained by taking the differential from equations (21) and (23) with respect to V which yields

$$\frac{d\phi_{T_{m1}}}{dV} = \frac{\partial \phi_{T_{m1}}}{\partial V} + \frac{\partial \phi_{T_{m1}}}{\partial x_m} \frac{dx_m}{dV} + \frac{\partial \phi_{T_{m1}}}{\partial z_m} \frac{dz_m}{dV} + \frac{\partial \phi_{T_{m1}}}{\partial h_0} \frac{dh_0}{dV} = 0, \quad (26)$$

$$\frac{d\phi_{T_{m2}}}{dV} = \frac{\partial \phi_{T_{m2}}}{\partial V} + \frac{\partial \phi_{T_{m2}}}{\partial x_m} \frac{dx_m}{dV} + \frac{\partial \phi_{T_{m2}}}{\partial z_m} \frac{dz_m}{dV} + \frac{\partial \phi_{T_{m2}}}{\partial h_0} \frac{dh_0}{dV} = 0. \quad (27)$$

In the LPD process the clad height and scanning speed are related to each other. By considering a parabolic shape for the clad (see figure 2) and applying the mass balance rule, the clad height is obtained by

$$h_0 = \frac{3\alpha_{\text{powder}}\dot{m}}{2\rho_{\text{powder}}w_0V}, \quad (28)$$

where α_{powder} is powder catchment efficiency, \dot{m} is powder flow rate (kg s⁻¹) and ρ_{powder} is powder density (kg m⁻³).

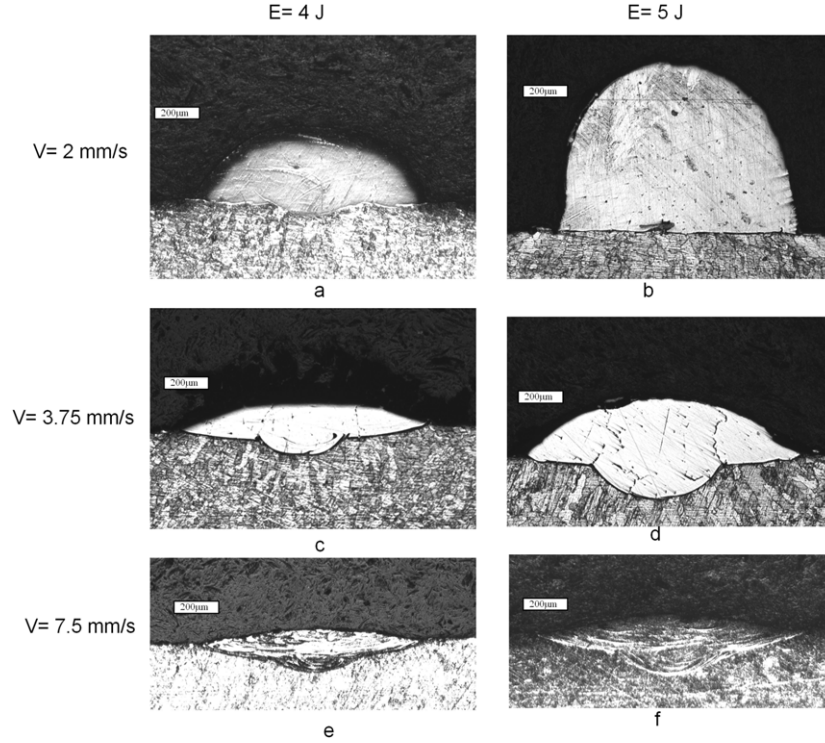


Figure 11. Cross sections of the clad at different process parameter at $F = 90$ Hz, $\dot{m} = 2$ g min⁻¹.

By taking the differential from the above equation with respect to scanning speed, it yields

$$\frac{dh_0}{dV} = -\frac{3\alpha_{\text{powder}}\dot{m}}{2\rho_{\text{powder}}w_0V^2}. \quad (29)$$

By considering equations (25)–(28), the critical scanning speed can be obtained as

$$V_{\text{cr}} = \sqrt{\frac{3\alpha_{\text{powder}}\dot{m}}{2\rho_{\text{powder}}w_0}} \times \frac{J_2}{J_1}, \quad (30)$$

where J_1 and J_2 are the Jacobians as follows:

$$J_1 = \left| \frac{\partial(\phi_{T_{m1}}, \phi_{T_{m2}})}{\partial(x, V)} \right|, \quad (31)$$

$$J_2 = \left| \frac{\partial(\phi_{T_{m1}}, \phi_{T_{m2}})}{\partial(x, h_0)} \right|. \quad (32)$$

According to figures 9 and 10 the increasing rate of the melt pool depth is more than its decreasing rate so that the melt pool depth decreases slowly with increasing scanning speed. This behaviour is because of the clad height variation. According to figure 6, the clad height decreases with a higher rate at velocities lower than the critical scanning speed.

Figure 11 depicts the cross section of some tracks at different laser power and scanning speed. As the figure clearly indicates, at lower velocities the melt pool depth is very small (figures 11(a) and (b)) and with the increase of the scanning speed the melt pool depth increases. This low melt pool depth at low speed results from the blocking effect, and for high speed the decrease in the melt pool depth is due to the lower interaction time between the laser beam and the deposited materials.

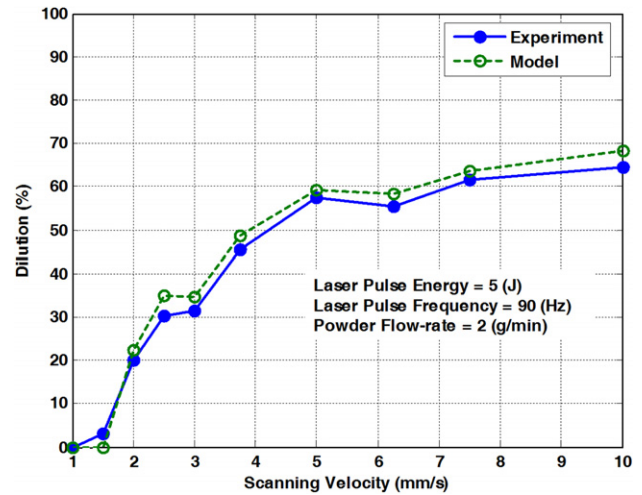


Figure 12. Dilution variation as a function of scanning speed; $E = 5$ J, $F = 90$ Hz, $\dot{m} = 2$ g min⁻¹.

It should be noted that the maximum of the melt pool depth does not necessarily result in a maximum of dilution. Figure 12 shows the model prediction and experimental results of dilution variation in terms of the scanning speed when the laser power and powder flow-rate are constant. As the figure indicates, the dilution increases with increasing scanning speed with a saturated limit and a nonlinear behaviour. This figure indicates that the dilution is more sensitive at lower scanning speed. According to this figure, the proposed model can predict the dilution with very good accuracy.

In figure 13, the melt pool depth contours are plotted at different values of scanning speed and clad height in the case of

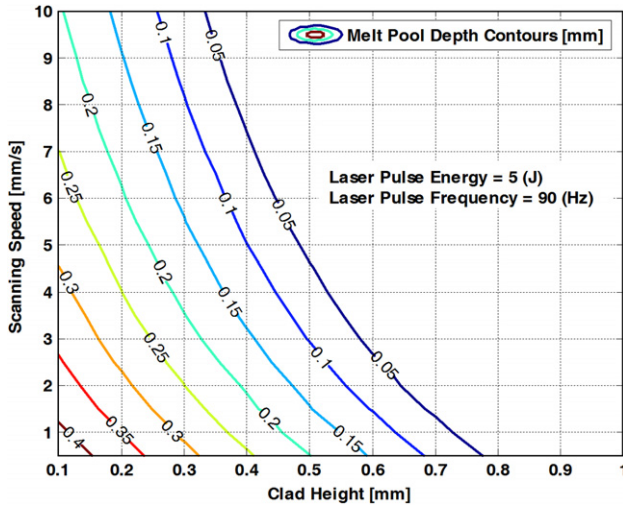


Figure 13. General map of the melt pool depth variation according to clad height and scanning speed variations at $E = 5$ J and $F = 90$ Hz.

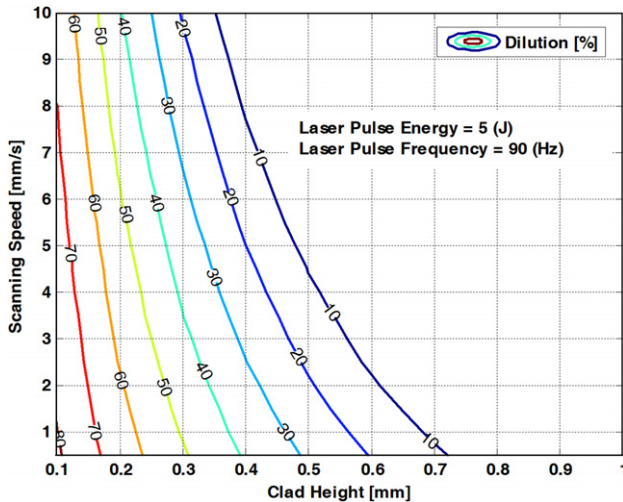


Figure 14. General map of dilution prediction as a function of clad height and scanning speed at $E = 5$ J and $F = 90$ Hz.

the stainless steel powder cladding on the mild steel substrate. These curves, which are obtained by the proposed model, can be used for the melt pool depth prediction. As the figure shows, the maximum value of the melt pool depth occurs at low clad heights and low laser beam velocities. Knowing the clad height and scanning speed, the melt pool depth can be predicted from this figure. Similarly, figure 14 shows the dilution variation as a function of the clad height and scanning speed. Using this figure and based on the amount of desirable dilution, a specific domain is determined that can then be used for process control purposes. The controller should tune the process parameters such that the mean value of dilution remains in a specific domain.

Figure 15 shows the steady state temperature field in the cross-section plane (x - z) at ($y = 0$) and cross-section plane x - y at $z = -0.01$ mm where the laser beam centre is located at $x = 0$. As shown, in the longitudinal plane, the shape of the isotherm is not symmetric with respect to the laser

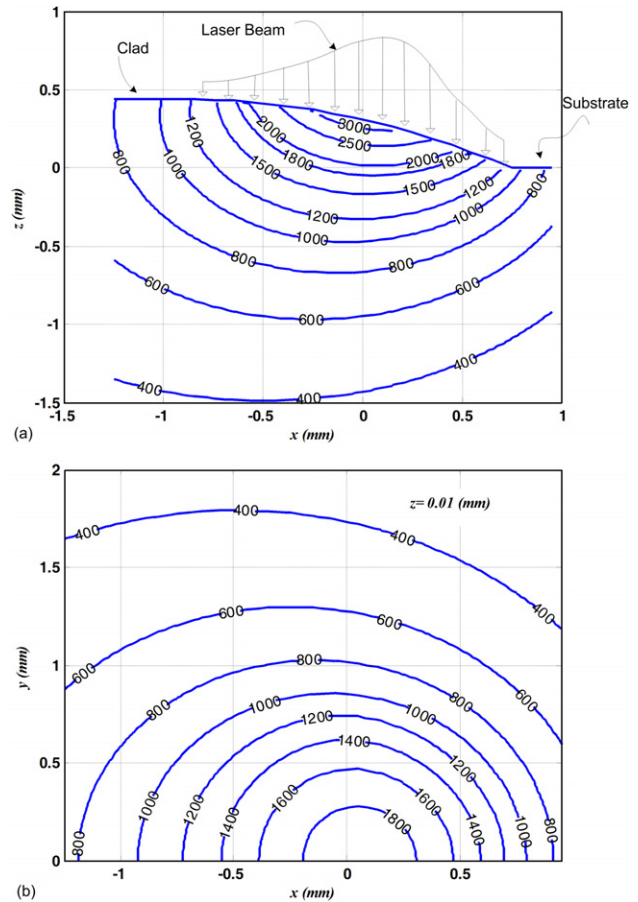


Figure 15. Temperature distribution ($^{\circ}\text{C}$) in the melt pool, clad and substrate, (a) longitudinal cross-section plane (x - z) at ($y = 0$), (b) transverse cross-section plane (x - y) at ($z = -0.01$ mm); $E = 5$ J, $F = 90$ Hz.

beam centreline because of the moving heat source. Since equations (19) and (20) are symmetric with respect to y , the deepest point of the melt pool is located on the longitudinal plane ($y = 0$).

In applications where the laser beam only irradiates on a planar surface (e.g. laser surface hardening), the deepest point of each isotherm line occurs behind the laser beam centreline. In the laser cladding process; however, at low temperature (i.e. lower than 800°C) this behaviour is observed but as the temperature increases, the deepest part of the melt pool moves to the front side of the laser beam centreline. As seen in figure 15, the deepest point for $T = 1500^{\circ}\text{C}$ is at $x = 0.0$ mm while for $T = 400^{\circ}\text{C}$ it is at $x = -0.5$ mm. This nature, in fact, is due to the contribution of the generated clad height to the modelling.

Figure 16 shows the variations of the interface temperature and its cooling/heating rate with respect to time at different clad heights, scanning speeds and constant laser power. According to this figure, at constant clad height and laser power, the cooling/heating rate increases. Also this figure indicates that with increasing clad height the cooling/heating rate decreases. Since the microstructure of the deposited material is very dependent on the cooling/heating rate, we can control the metallurgical properties of the clad/substrate by using this model for predicting the cooling/heating rate.

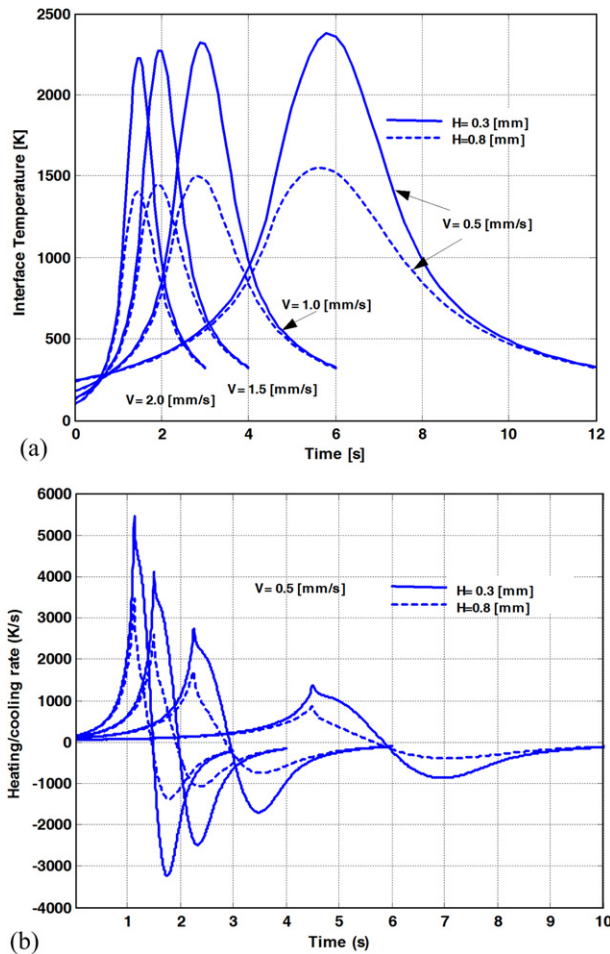


Figure 16. (a) Interface temperature variation and (b) interface cooling/heating rate at different scanning speeds and clad heights and constant laser power ($E = 5$ J, $F = 90$ Hz).

Figure 17 indicates the effects of the laser beam power on the melt pool depth and the dilution. As this figure shows, both melt pool depth and dilution increase with increasing laser beam energy. This is evident, because with increasing laser power, there is more energy available for melting the substrate.

In summary, since the model is not computationally intensive, it can effectively be used in a real-time control of the process. The frequency rate of the code developed based on the proposed model is about 40 Hz, which is higher than the frequency of the vision-based control system (i.e. 30 Hz). Hence the incorporation of the developed model into the control system is feasible. For future work, this model will be integrated in the existing control system to adaptively tune the process parameters in real-time to arrive at the desired dilution in the process.

4. Conclusion

In this study, a new 3D mathematical model for predicting the melt pool geometry and dilution was developed. The output of this integral form model showed that the melt pool depth has a non-linear behaviour such that it has a maximum at a certain process speed. Also the numerical and experimental results

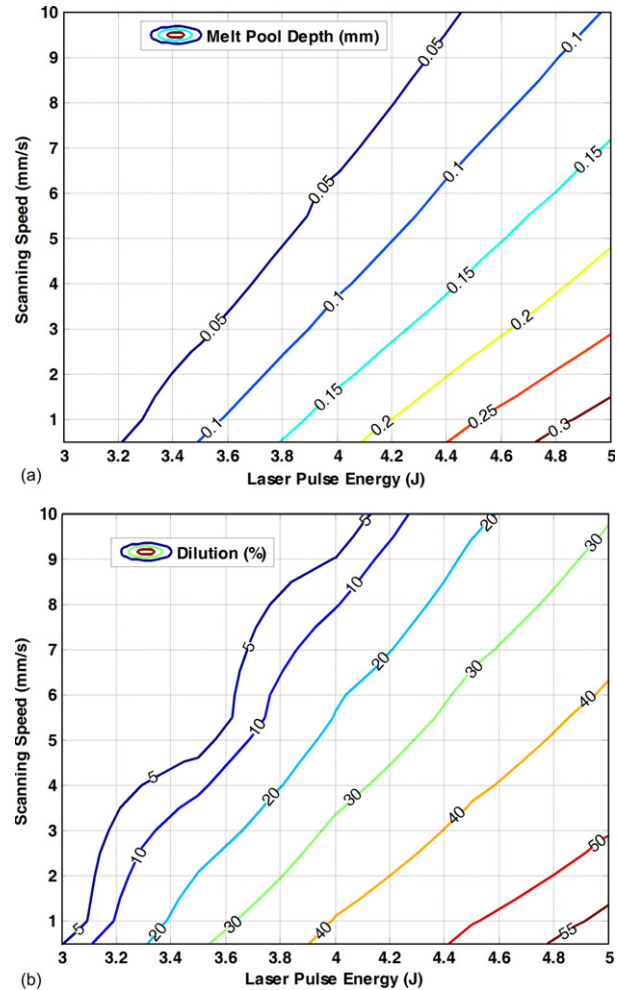


Figure 17. Effect of laser beam energy on (a) melt pool depth, and (b) Dilution at a constant clad height ($H = 0.5$ mm).

showed that the dilution has a nonlinear nature with respect to scanning speed. Based on this model some general curves were developed for use in the prediction of the melt pool depth and dilution in terms of clad height and the scanning speed. The effects of the laser beam energy and the clad height (which is a function of powder feed-rate) on the melt pool depth and dilution were studied. The results showed that with increasing laser beam power, both the melt pool depth and the dilution increase and vice versa. The experimental verification showed that this model is capable of predicting the characteristics of the laser powder process accurately.

References

- [1] Toyserkani E, Khajepour A and Corbin S F 2004 *Laser Cladding* (Boca Raton, FL: CRC Press) ISBN: 0-8493-2172-7
- [2] Jeng J-Y and Lin M-C 2001 Mold fabrication and modification using hybrid processes of selective laser cladding and milling *J. Mater. Process. Technol.* **110** 98–103
- [3] Liu W and DuPont J N 2003 Fabrication of functionally graded TiC/Ti composites by laser engineered net shaping *Scripta Mater.* **48** 1337–42
- [4] Picasso M and Hoadley A F A 1994 Finite element simulation of laser surface treatments including convection in the melt pool *Int. J. Numer. Methods Heat Fluid Flow* **4** 61–83

-
- [5] Hoadley A F A and Rappaz M 1992 A thermal model of laser cladding by powder injection *Metall. Trans. B* **23** 631–42
 - [6] Mazumder J and Steen W M 1980 Heat transfer model for cw laser material processing *J. Appl. Phys.* **51** 941–7
 - [7] Chan C, Mazumder J and Chen M M 1983 Two-dimensional transient model for convection in laser melted pool *Metall. Trans. A* **15** 2175–84
 - [8] Han L, Liou F W and Phatak K M 2004 Modeling of laser cladding with powder injection *Metall. Mater. Trans. B: Process Metall. Mater. Process. Sci.* **35** 1139–50
 - [9] Toyserkani E, Khajepour A and Corbin S 2003 Three-dimensional finite element modeling of laser cladding by powder injection: Effects of powder feedrate and travel speed on the process *J. Laser Appl.* **15** 153–60
 - [10] Toyserkani E, Khajepour A and Corbin S 2004 3-D finite element modeling of laser cladding by powder injection: Effects of laser pulse shaping on the process *Opt. Lasers Eng.* **41** 849–67
 - [11] Pinkerton A and Li L 2004 Modelling the geometry of a moving laser melt pool and deposition track via energy and mass balances *J. Phys. D: Appl. Phys.* **37** 1885–95
 - [12] Hofmeister W, Griffith M, Ensz M and Smugeresky J 2001 Solidification in direct metal deposition by LENS processing *JOM* **53** 30–4
 - [13] Gedda H, Powell J, Wahlstrom G, Li W-B, Engstrom H and Magnusson C 2002 Energy redistribution during CO₂ laser cladding *J. Laser Appl.* **14** 78–82
 - [14] Carslaw H S and Jaeger J C 1959 *Conduction of Heat in Solids* 2nd edn (Oxford: Oxford University Press)
 - [15] Steen W M 1998 *Laser Material Processing* (Berlin: Springer)
 - [16] Lampa C, Kaplan A F H, Powell J and Magnusson C 1997 Analytical thermodynamic model of laser welding *J. Phys. D: Appl. Phys.* **30** 1293–9
 - [17] Brown S and Song H 1992 Finite element simulation of welding of large structures *J. Eng. Ind. Trans. ASME* **114** 441–51
 - [18] ASM International Materials Properties Database Committee 2002 *Thermal Properties of Metals* (ASM International)
 - [19] Xie J and Kar A 1997 Mathematical modeling of melting during laser materials processing *J. Appl. Phys.* **81** 3015–22